This is the peer-reviewed, final accepted version for American Mineralogist, published by the Mineralogical Society of America.
The published version is subject to change. Cite as Authors (Year) Title. American Mineralogist, in press.
DOI: https://doi.org/10.2138/am-2022-8636. http://www.minsocam.org/

Revision 1 **Word Count: 5026**

Enrichment of precious metals associated with chalcopyrite inclusions in sphalerite and pyrite

He Zhang[1,2], Gujie Qian[2], Fengfang Zhou[3], Yuanfeng Cai[1,*], Allan Pring[2,4,*]

[1]State Key Laboratory of Mineral Deposit Research, School of Earth Sciences and Engineering, Nanjing University, Nanjing 210023, China
[2]College of Science and Engineering, Flinders University, Bedford Park, Adelaide, SA 5042, Australia
[3]College of Mechanical and Electronic Engineering, Nanjing Forestry University, Nanjing 210037, China
[4]Department of Earth Sciences, University of Adelaide, Adelaide, SA 5005, Australia

ABSTRACT

The results of investigations into enrichment of precious metals in sphalerite and pyrite from the Maluntou epithermal gold deposit, China are reported. The resulting data suggest intimate associations of Au- and Ag-bearing nanoparticles with chalcopyrite inclusions in sphalerite and pyrite. The origins of chalcopyrite inclusions involved different hydrothermal processes, including recrystallization-driven phase separation from parent chalcopyrite-sphalerite solid-solutions, and replacement of pre-existing pyrite in the presence of Cu-bearing fluids. The chalcopyrite blebs/lamellae follow sphalerite {111} planes which define a shared sulfur layer for both chalcopyrite and sphalerite. This study indicates that mixing and boiling during evolution of ore-forming fluids for the Maluntou deposit are key processes for the abnormal enrichment of precious metals in sphalerite and pyrite. The chalcopyrite micro/nano inclusions enhanced enrichment of precious metals in sphalerite provides new insights into the controls on the enrichment of precious metals in sulfides.

Keywords: chalcopyrite inclusion, precious metal, sphalerite, epithermal gold deposit

INTRODUCTION

Of the major precious metals recovered from sulfide ore deposits, gold and silver show natural affinities with different sulfide minerals. Gold is unique in that it occurs as both "visible" grains (>1000 Å; under aided optical magnification) and "invisible" (<1000 Å) Au in pyrite, with the latter either entrapped into the lattice defects as nanoparticles (Au^0) or incorporated into the pyrite structure in solid solutions (Au^{1+}; Cook and Chryssoulis, 1990; Palenik et al., 2004; Reich et al., 2005; Hastie et al., 2021). In contrast, Ag is usually recovered as a by-product in Pb and Zn mining of hydrothermal Pb-Zn deposits (Slack et al., 2020; Belokonov et al., 2021), as Ag has an affinity with galena and sphalerite (Huston et al., 1996; Wu et al., 2016, 2018); although high concentrations of Ag are more likely related to μm/sub-μm sized inclusions of discrete argentiferous sulfosalts, such as diaphorite (Sharp and Buseck, 1993; Giuli et al., 2005) and tetrahedrite (Gasparrini and Lowell, 1985; Wang et al., 2018; Zhai et al., 2019) in galena.

Several mechanisms are thought to control the incorporation of Au and Ag as solid solutions in sulfides. Arsenic-induced defects have been proposed to facilitate the incorporation of Au in arsenian pyrite (Gopon et al., 2019; Zhang et al., 2022), with substitution of Au^{1+} for Fe^{2+} (Merkulova et al., 2019; Filimonova et al., 2020; Meng et al., 2022). Galena can host significant quantities of Ag^{1+}, through the following coupled substitutions of $Ag^{1+} + Sb^{3+} \Leftrightarrow 2Pb^{2+}$ or $Ag^{1+} + Bi^{3+} \Leftrightarrow 2Pb^{2+}$ (Lueth et al., 2000; Chutas et al., 2008; Grant et al., 2015). Silver(I) can enter the

chalcopyrite structure via a co-substitution mechanism: $(x + 2y)(Ge, Sn)^{4+} + x(Zn, Pb)^{2+} + y(Cu, Ag)^{1+} \Leftrightarrow (2x + 3y)Fe^{3+}$ (Belissont et al., 2019) and can also be incorporated into the sphalerite structure through limited coupled substitutions via $2Ag^{1+} + Sn^{4+} \Leftrightarrow 3Zn^{2+}$ (Cook et al., 2009) or $Ag^{1+} + Cu^{1+} + Sn^{4+} \Leftrightarrow 3Zn^{2+}$ (Pring et al., 2020). Furthermore, geochemical factors likely influence the distribution of Ag in sulfides. For example, higher temperatures and more reduced conditions favor preferential partitioning of Ag into chalcopyrite over galena and sphalerite in hydrothermal systems (Huston et al., 1996; Wu et al., 2016).

In recent years, there has been a growing attention towards the role of submicron- to nanometer-sized mineral particles in controlling the mobility of precious metals in geological settings (e.g., Reich et al., 2006; Deditius et al., 2011; Wu et al., 2016, 2018). The disseminated chalcopyrite in sphalerite crystals has been extensively documented from natural ores of sulfide deposits (e.g., Bortnikov et al., 1991; Xu et al., 2021). Here, we document enhanced enrichment of precious metals in sphalerites by chalcopyrite micro/nano inclusions, relative to those chalcopyrite-free sphalerites from the Maluntou epithermal gold deposit, which provides new insights into the controls on the enrichment of precious metals in sulfides.

MATERIALS AND METHODS

Materials

Maluntou deposit is an intermediate-sulfidation epithermal Au deposit (> 5.0 t Au @ 3.70 g/t) in the Dongkeng Volcanic Basin in Fujian Province, southeastern China, where ore-forming fluids evolved from higher-temperature magmatic-hydrothermal

This is the peer-reviewed, final accepted version for American Mineralogist, published by the Mineralogical Society of America.
The published version is subject to change. Cite as Authors (Year) Title. American Mineralogist, in press.
DOI: https://doi.org/10.2138/am-2022-8636. http://www.minsocam.org/

fluids (up to 377 °C) due to mixing with meteoric water (Chen et al., 2021). The orebodies are hosted by hydrothermally-altered volcanic breccias and dacitic-rhyolitic pyroclastic rocks of the Huangkeng Formation and spatially controlled by the NW- and NE-striking faults and fractures (Chen et al., 2021). Ore samples used in this study (Fig. 1) were collected from the altered dacitic volcanic tuff at 360 m above sea level.

Electron Microprobe Analysis

The chemical composition of sphalerite was determined using electron microprobe analysis (EMPA) employing a JXA 8230 instrument. The microprobe is equipped with five wavelength-dispersive X-ray spectrometers (WDS), including channel 1 (PETJ and LiF), channel 2 (TAP and LDE2), channel 3 (PETH and LiFH), channel 4 (PETL and LiFL), and channel 5 (TAP and LDE1). Elements, X-ray lines and standards used were: Fe*Kα*/chalcopyrite, Cu*Kα*/chalcopyrite, Zn*Kα*/sphalerite, Pb*Mα*/galena, S*Kα*/spahlerite, As*Lα*/arsenopyrite, Au*Mα*/metallic gold, Sb*Lα*/Sb_2Te_3, Ni*Kα*/$(Fe,Ni)_9S_8$, Ag*Lα*/metallic silver, and Mn*Kα*/fayalite (2.2 wt% MnO). A LiF crystal was used for Fe, Cu, and Zn, a PETJ crystal for Pb and S, a TAP crystal for As, a PETH crystal for Au and Sb, a LiFH crystal for Ni, a PETL crystal for Ag, and a LiFL crystal for Mn. The analyses were undertaken using an accelerating voltage of 15 kV and a beam current of 20 nA. The beam spot diameter was set at 1 μm.

TESCAN Integrated Mineral Analysis

TESCAN Integrated Mineral Analysis (TIMA) can deliver high speed, detailed measurements on samples by using multiple energy dispersive X-ray spectroscopy

(EDS) detectors operated at very high count rates, provide quantitative data for mineral identification, and help further understand complex mineral relationships (e.g., Hrstka et al., 2018). Here, compositional maps were obtained on carbon-coated thin sections using a TESCAN Mira-3 field emission scanning electron microscope (FE-SEM) equipped with four EDS detectors (EDAX Element 30) at Nanjing Hongchuang Geological Exploration Technology Service Co. Ltd., China. An acceleration voltage of 25 kV and a probe current of 9.25 nA were used. The electron beam intensity was set to 19.00 and spot size to 86.99 nm. Working distance was set to 15 mm. Before every test, the probe current and backscattered electron (BSE) signal intensity were calibrated on a Faraday cup using the automated procedure. The calibration set point was 600 kcps. EDS performance was checked using a manganese standard. This dot mapping mode, together with TIMA liberation analysis, was used to collect modal and textural data of our samples. The pixel and dot spacings were set to 3 μm and 9 μm, respectively. 160 individual fields with 1500 μm width were scanned, with X-ray events and acquisition pts being 4690.6 M and 4766156, respectively.

Transmission Electron Microscopy

A carbon-coated thin section was characterized by optical and SEM microscopy prior to focused ion beam-SEM (FIB-SEM) study. Two foils from the chalcopyrite-speckled areas of sphalerite were prepared using a Helios G4-UX dual FIB-SEM at Nanjing NanZhi Institute of Advanced Optoelectronic Integration, China. The sample was first tilted at 52° with respect to the ion beam. The procedure starts

by the deposition of platinum onto the region of interest to prevent damage of the top portion of the specimen during milling. Trenches were sputtered on either side of the region of interest using a Ga^+ ion-beam at high voltage and current (30 kV and 20 nA) to produce a slice, with its two surfaces cleaned using a lower current (0.79 nA). The specimen was then de-tilted to 0^o and a tungsten needle was brought into the field and welded with Pt onto the top portion of the slice. The slice was then lifted, transported, and finally attached to the Cu grid holder and the needle was cut away. The specimen was tilted back to 52^o and milling was conducted on alternate sides of the slice using various beam currents (80 pA – 0.79 nA). The foil was finally cleaned at low voltage and current (5 kV and 15 pA) and polished to a final thickness of ~ 80 nm.

Two foils were imaged using a FEI Tecnai F20 transmission electron microscope (TEM) and a FEI Titan Cubed G2 60−300 aberration-corrected S/TEM (equipped with Super-X™ technology) at Nanjing University, China. The two instruments were operated at electron beam accelerating potentials of 200 kV and 300 kV, respectively. Bright-field TEM observations, selected-area electron diffraction (SAED), high-angle annular dark-field (HAADF) observations, and EDS analyses (~ 1 wt% detection limit) were performed. The latter two observations and analyses were performed under scanning TEM (STEM) mode. The 22.5 mrad convergence angle and 0.05 nA probe current were used for the HAADF-STEM observations.

RESULTS

The texture of a typical ore sample from the Maluntou deposit clearly exhibits three distinct features: quartz veins, alteration zones, and dacitic volcanic tuff (Fig. 1).

TIMA mapping show that sulfides are enriched within the alteration zones (Fig. 1a) and predominantly composed of sphalerite and galena, with minor chalcopyrite and pyrite (Fig. 1b).

Most sphalerite crystals are heavily speckled with chalcopyrite blebs/lamellae in the μm to sub-μm size range (Fig. 2). Such a texture is sometimes referred to as "chalcopyrite disease" (Barton, 1978). A higher magnification view of the texture shows that the distributions of some chalcopyrite lamellae are crystallographically controlled (Figs. 2e and 2f). In addition, some sphalerite domains show the absence of chalcopyrite inclusions (Figs. 2e and S1) and range from approximately several microns to 500 μm in size on the basis of Figure S1. Further EMPA analysis indicates that sphalerite is Fe-bearing (0.1–2 wt%) and Au/Ag-free (Table S1). At least 80% of the total chalcopyrite in our sample occurs as blebs/lamellae in sphalerite, while the remainder is present as fracture-fillings in pyrite (Figs. 2g and 2h).

The intimate intergrowths of electrum with either chalcopyrite or Ag-rich covellite were also found in pyrite (Figs. 2g, 2h, S2, and S3). The Raman spectrum confirms that the mineral is covellite rather than "blaubleibender covellin" species, yarrowite or spionkopite. Together with Cu enrichment, minor amounts of Cu-Ag-(Au) nanoparticles are adhered to those chalcopyrite inclusions in sphalerite (Figs. 2c and 2d), providing an evidence of the derivation of the precious metals from Cu-rich hydrothermal fluids.

Further TEM observations suggest the presence of dislocation/stacking fault-induced distortions (Fig. 3). These distortions are arranged parallel to one

another and follow {111} planes (Figs. 3a and 3e–3f). The crystallography-constrained distribution of chalcopyrite lamellae in sphalerite is evident, with the lamellae following sphalerite {111} planes (Figs. 3b–3e). In addition, the chalcopyrite blebs/lamellae are closely associated with nanoparticles of native Cu, Au-Ag-Cu alloy and Cu-Ag-S, as indicated by EDS mappings (Figs. 4, S4 and S5).

DISCUSSION

Possible origins of chalcopyrite blebs/lamellae within sphalerite

The origin of disseminated chalcopyrite blebs/lamellae in sphalerite remains unclear and possibly involves processes of exsolution (Shimazaki, 1980), replacement (Govindarao et al., 2018), coprecipitation (Bortnikov et al., 1991) or a mixture of the above. Given hydrothermal origins of these blebs/lamellae, some empirical arguments, such as extremely limited Cu solubility in sphalerite (Kojima and Sugaki, 1984) based on dry experiments at relatively high temperatures (> 500 ^{o}C) rather than under hydrothermal conditions, require further mineralogical re-examination built on mineralogical textural evidence. Exsolution of chalcopyrite from bornite (Li et al., 2018; Adegoke et al., 2021), and bornite from bornite-digenite solid-solutions (Zhao et al., 2017), in the presence of hydrothermal fluids has been reported to be greatly accelerated compared to the equivalent dry system at lower temperatures (< 300 ^{o}C). The exsolution rate and lamellae size were found to be very sensitive to the compositions of hydrothermal fluids. Here, replacement is unlikely to be the mechanism for our sphalerites where most chalcopyrite occurs as μm/sub-μm sized inclusions (Figs. 2 and S1), without typical hydrothermal replacement textures (e.g.,

chalcopyrite mesh-veinlets; Xu et al., 2021). In contrast, replacement is evident for pyrite where chalcopyrite occurs as fracture-fillings (Figs. 2g and 2h). Additionally, the intimate association of Cu-Ag-(Au) nanoalloys and chalcopyrite blebs/lamellae (Figs. 2c and 2d) is indicative of a common formation mechanism. Zhao et al. (2017) reported a process of hydrothermal and recrystallization-driven coarsening of exsolution lamellae from bornite-digenite solid-solutions, which was accompanied by healing of open porous microstructures in the solid-solutions. Li et al. (2018) observed a similar situation with the exsolution of chalcopyrite from bornite. Wu et al. (2018) also reported a recrystallization-driven decrease in Ag content, mineral porosity, and defect density within natural sphalerite from the Edmond hydrothermal field, Central Indian Ridge. Temperature-dependent structural transformation was identified from the tetragonal α-phase chalcopyrite into the high-temperature cubic β-phase above 400 ^{o}C (Baláž et al., 1989; Chang et al., 2019). Based on these findings, it is likely that these chalcopyrite blebs/lamellae resulted from hydrothermal recrystallization, with phase separation, where earlier coprecipitation of metastable chalcopyrite-sphalerite solid-solution phases was possibly followed by a fluid-driven recrystallization process to eliminate intragranular porosity (Fig. 2d). The decreased porosity, in turn, caused a shortened path length for rapid solid-solution diffusion. Crystal-chemical considerations suggest that intragranular diffusion tends to be crystallographically constrained (e.g., Fougerouse et al., 2016). The extension of chalcopyrite lamellae along sphalerite {111} planes is evident in our study (Fig. 3). The alternative stacking structures of sulfur and metal atoms layers along sphalerite

[111] or chalcopyrite [001]/[112] can facilitate epitaxial crystallization of chalcopyrite following sphalerite {111} planes. Similar links have also been documented in the reaction of chalcopyrite with hydrochloric acid where nantokite lamellae followed the chalcopyrite {001} and {112} planes which define a shared Cu layer for both chalcopyrite and nantokite (Cai et al., 2012).

Natural chalcopyrite can form by replacing pyrite in Cu-bearing hydrothermal fluids based on geological observations (Wu et al., 2016) and experimental investigations (Zhang et al., 2020, 2021), although limited amounts of Cu can substitute Fe into the pyrite structure (Pačevski et al., 2008). Therefore, the difference in occurring modes of chalcopyrite (blebs/lamellae vs. fracture-fillings; Fig. 2) can be regarded as a reflection of different mineral reaction processes, including recrystallization-driven phase separation from parent chalcopyrite-sphalerite solid-solutions, and replacement of pre-existing pyrite in the presence of Cu-bearing fluids.

Controls on enrichment of precious metals within sphalerite

The "barren" sphalerite domains are Au/Ag-free, consistent with general findings that sphalerite is not a significant host for structurally-bound Ag in hydrothermal systems, unless through coupled substitutions of Ag^{1+}, with cations such as Sn^{4+} or In^{3+}, for Zn^{2+} (Cook et al., 2009; Pring et al., 2020). Here, the intimate intergrowths of chalcopyrite blebs/lamellae with Cu-Ag-(Au) nanoparticles not only provide evidence of chalcopyrite micro/nano inclusions enhanced enrichment of precious metals within sphalerite but are also the best indicators of a key role of "chalcopyritization" in

scavenging precious metals in epithermal systems. Similarly, the introduction of electrum grains into pyrite is frequently accompanied by chalcopyritization, such as those reported in the Qiucun low-sulfidation (Ni et al., 2018; Zhang et al., 2022), the Dongji intermediate-sulfidation (Chen et al., 2021), and the Zijinshan high-sulfidation epithermal deposits (Liu et al., 2016).

Of particular note is that the different modes of occurrence of Ag (ionic vs. particulate) in covellite and chalcopyrite (Figs. 2c and 2h), respectively, are consistent with the facts that gold and other precious metals readily exsolve at low temperatures from chalcopyrite, in contrast to covellite which has stronger ability to withstand cooling (Fraley and Frank, 2014; Tagirov et al., 2016). The covellite is generally of secondary origin in zones of oxidation and secondary enrichment of sulfide ore deposits and derives from primary sulfides such as chalcopyrite (e.g., Liu et al., 2016). The occurrence of Ag-rich covellite is also inferred to result from input of oxygenated seawater in some submarine hydrothermal fields and volcanic-related hydrothermal ore deposits (Demir et al., 2013; Melekestseva et al., 2017). In this study, the upwelling ore-forming fluids for the Maluntou deposit are expected to evolve into a system of relatively lower sulfur fugacity and higher oxygen fugacity. Mixing with oxygenated meteoric waters is an effective way of scavenging precious metals from ore-forming fluids, as a significant decrease in HS^{1-} concentration can result from a relatively small increase in oxygen fugacity, thereby de-stabilizing metal hydrosulfide complexes (Williams-Jones et al, 2009). Fluid boiling is also another effective way to reduce the HS^{1-} concentration and temperature through phase separation and adiabatic

248 expansion, respectively (Heinrich, 2007). Such processes of mixing and boiling have
249 recently been proposed to occur during the evolution of ore-forming fluids at the
250 Maluntou deposit based on analyses of fluid inclusions and petrography (Chen et al.,
251 2021). Chen et al., (2021) also proposed that this may have triggered the
252 coprecipitation of metal ions from the Maluntou ore-forming fluids and promoted the
253 enrichment of precious metals within chalcopyrite-sphalerite solid-solutions.

254 **IMPLICATIONS**

255 This study highlights the key role played by chalcopyrite inclusions in enhancing
256 the enrichment of precious metals in sphalerite and pyrite. Such information can help
257 in understanding the geochemical behaviors of Au, Ag, and Cu during the evolution of
258 epithermal ore-forming fluids, and thereby provide guidance for further ore
259 prospecting.

260 The diversity of distribution and mode of occurrence of precious metals in
261 sulfides involves a range of different hydrothermal processes, such as replacement
262 and recrystallization-driven phase separation. Systematic research can characterize the
263 distribution of precious metals in sulfides, especially those in ores where fluid boiling
264 or mixing with oxygenated meteoric waters has occurred. Such information is critical
265 for understanding Au/Ag recovery and industry processing of refractory ores.

266

267 **ACKNOWLEDGEMENTS**

268 This study was financially supported by three NSFC projects (Grants 42192504,
269 41272055, and 41830426). We are grateful to Juan Li for assistance during SEM

imaging, Li Li and Weihao Yan for assistance with TIMA, Ruomu Li for assistance with FIB-SEM analysis, Wenlan Zhang for assistance with EMPA, and Jiani Chen and Zhichao Wang for TEM analysis. This paper greatly benefited from constructive comments and thorough reviews from two anonymous refrees.

REFERENCES CITED

Adegoke, I.A., Xia, F., Deditius, A.P., Pearce, M.A., Roberts, M.P., and Brugger, J. (2021) A new mode of mineral replacement reactions involving the synergy between fluid-induced solid-state diffusion and dissolution-reprecipitation: A case study of the replacement of bornite by copper sulfides. Geochimica et Cosmochimica Acta, 2022, 330, 165–190.

Baláž, P., Tkáčová, K., and Avvakumov, E.G. (1989) The effect of mechanical activation on the thermal decomposition of chalcopyrite. Journal of thermal analysis, 35, 1325–1330.

Barton, P.B. Jr. (1978) Some ore textures involving sphalente from the Furutobe mine, Akita Prefecture, Japan. Mining Geology, 28, 293–300.

Belissont, R., Munoz, M., Boiron, M.C., Luais, B., and Mathon, O. (2019) Germanium crystal chemistry in Cu-bearing sulfides from micro-XRF mapping and micro-XANES spectroscopy. Minerals, 9, 227.

Belokonov, G., Frenzel, M., Priyatkina, N.S., Renno, A.D., Makarov, V., and Gutzmer, J. (2021) Geology and Genesis of the Giant Gorevskoe Pb-Zn-Ag Deposit, Krasnoyarsk Territory, Russia. Economic Geology, 116, 719–746.

Bortnikov, N.S., Genkin, A.D., Dobrovol'skaya, M.G., Muravitskaya, G.N., and

Filimonova, A.A. (1991) The nature of chalcopyrite inclusions in sphalerite: exsolution, coprecipitation, or "disease"? Economic Geology, 86, 1070–1082.

Cai, Y.F, Chen, X.M., Ding, J.Y., and Zhou, D.S. (2012) Leaching mechanism for chalcopyrite in hydrochloric acid. Hydrometallurgy, 113, 109–118.

Chang, K.X., Zhang, Y.S., Zhang, J.M., Li, T.F., Wang, J., and Qin, W.Q. (2019) Effect of temperature-induced phase transitions on bioleaching of chalcopyrite. Transactions of Nonferrous Metals Society of China, 29, 2183–2191.

Chen, M.T., Wei, J.H., Selby, D., Li, Y.J., Shi, W.J., and Zhao, Y.J. (2021) Cretaceous intermediate sulfidation ore system in the Dongkeng Volcanic Basin, SE China: constraints from the Dongji and Maluntou gold deposits. Ore Geology Reviews, 135, 104202.

Chutas, N.I., Kress, V.C., Ghiorso, M.S., and Sack, R.O. (2008) A solution model for high-temperature PbS-$AgSbS_2$-$AgBiS_2$ galena. American Mineralogist, 93, 1630–1640.

Cook, N.J., and Chryssoulis, S.L. (1990) Concentrations of invisible gold in the common sulfides. The Canadian Mineralogist, 28, 1–16.

Cook, N.J., Ciobanu, C.L., Pring, A., Skinner, W., Shimizu, M., Danyushevsky, L., Saini-Eidukat, B., and Melcher, F. (2009) Trace and minor elements in sphalerite: A LA-ICPMS study. Geochimica et Cosmochimica Acta, 73, 4761–4791.

Deditius, A.P., Utsunomiya, S., Reich, M., Kesler, S.E., Ewing, R.C., Hough, R., and Walshe, J. (2011) Trace metal nanoparticles in pyrite. Ore Geology Reviews, 42, 32–46.

Demir, Y., Uysal, İ., and Sadıklar, M.B. (2013) Mineral chemical investigation on sulfide mineralization of the Istala deposit, Gümüşhane, NE-Turkey. Ore Geology Reviews, 53, 306–317.

Filimonova, O.N., Tagirov, B.R., Trigub, A.L., Nickolsky, M.S., Rovezzi, M., Belogub, E.V., Reukov, V.L., and Vikentyev, I.V. (2020) The state of Au and As in pyrite studied by X-ray absorption spectroscopy of natural minerals and synthetic phases. Ore Geology Reviews, 121, 103475.

Fougerouse, D., Micklethwaite, S., Tomkins, A.G., Mei, Y., Kilburn, M., Guagliardo, P., Fisher, L.A., Halfpenny, A., Gee, M., and Paterson, D. (2016) Gold remobilisation and formation of high grade ore shoots driven by dissolution-reprecipitation replacement and Ni substitution into auriferous arsenopyrite. Geochimica et Cosmochimica Acta, 178, 143–159.

Fraley K.J., and Frank M.R. (2014) Gold solubilities in bornite, intermediate solid solution, and pyrrhotite at 500^{o} to 700 ^{o}C and 100 MPa. Economic Geology, 109, 407–418.

Gasparrini, C., and Lowell, G.R. (1985) Silver-bearing inclusions in" argentiferous" galena from the Silvermine District in southeastern Missouri. The Canadian Mineralogist, 23, 99–102.

Giuli, G., Paris, E., Wu, Z.Y., De Panfilis, S., Pratesi, G., and Cipriani, C. (2005) The structural role of Ag in galena (PbS). A XANES study. Physica Scripta, T115, 387–389.

Gopon, P., Douglas, J.O., Auger, M.A., Hansen, L., Wade, J., Cline, J.S., Robb, L.J.,

336 and Moody, M.P. (2019) A Nanoscale Investigation of Carlin-Type Gold Deposits:
337 An Atom-Scale Elemental and Isotopic Perspective. Economic Geology, 114,
338 1123–1133.
339 Govindarao, B., Pruseth, K.L., and Mishra, B. (2018) Sulfide partial melting and
340 chalcopyrite disease: An experimental study. American Mineralogist, 103, 1200–
341 1207.
342 Grant, H.L.J., Layton-Matthews, D., and Peter, J.M. (2015) Distribution and controls
343 on silver mineralization in the Hackett River Main Zone, Nunavut, Canada: An
344 Ag- and Pb-enriched Archean Volcanogenic Massive Sulfide Deposit. Economic
345 Geology, 110, 943–982.
346 Hastie, E.C.G., Schindler, M., Kontak, D.J., and Lafrance, B. (2021) Transport and
347 coarsening of gold nanoparticles in an orogenic deposit by dissolution–
348 reprecipitation and Ostwald ripening. Communications Earth & Environment, 2,
349 1–9.
350 Heinrich, C.A. (2007) Fluid-fluid interactions in magmatic-hydrothermal ore
351 formation. Reviews in Mineralogy and Geochemistry, 65, 363–387.
352 Hrstka, T., Gottlieb, P., Skála, R., Breiter, K., and Motl, D. (2018) Automated
353 mineralogy and petrology–applications of TESCAN Integrated Mineral Analyzer
354 (TIMA). Journal of Geosciences, 63, 47–63.
355 Huston, D.L., Jablonski, W., and Sie, S.H. (1996) The distribution and mineral hosts
356 of silver in eastern Australian volcanogenic massive sulfide deposits. Canadian
357 Mineralogist, 34, 529–546.

358 Kojima, S., and Sugaki, A. (1984) Phase relations in the central portion of the
359 Cu-Fe-Zn-S system between 800° and 500 °C. Mineralogical Journal, 12, 15–28.
360 Li, K., Brugger, J., and Pring, A. (2018) Exsolution of chalcopyrite from
361 bornite-digenite solid solution: An example of a fluid-driven back-replacement
362 reaction. Mineralium Deposita, 53, 903–908.
363 Liu, W.Y., Cook, N.J., Ciobanu, C.L., Liu, Y., Qiu, X.P., and Chen, Y.C. (2016)
364 Mineralogy of tin-sulfides in the Zijinshan porphyry–epithermal system, Fujian
365 Province, China. Ore Geology Reviews, 72, 682–698.
366 Lueth, V.W., Megaw, P.K.M., Pingitore, N.E., and Goodell, P. C. (2000) Systematic
367 variation in galena solid-solution compositions at Santa Eulalia, Chihuahua,
368 Mexico. Economic Geology, 95, 1673–1687.
369 Melekestseva, I.Y., Maslennikov, V.V., Maslennikova, S.P., Danyushevsky, L.V., and
370 Large, R. (2017). Covellite of the Semenov-2 hydrothermal field (13^{o} 31.13′ N,
371 Mid-Atlantic Ridge): Enrichment in trace elements according to LA ICP MS
372 analysis. Doklady Earth Sciences. Pleiades Publishing, 473, 291–295.
373 Meng, L., Zhu, S.Y., Li, X.C., Chen, W.T., Xian, H.Y., Gao, X.Y., and Zhao, T.P.
374 (2022) Incorporation mechanism of structurally bound gold in pyrite: Insights
375 from an integrated chemical and atomic-scale microstructural study. American
376 Mineralogist, 107, 603–613.
377 Merkulova, M., Mathon, O., Glatzel, P., Rovezzi, M., Batanova, V., Philippe, M.,
378 Boiron, M.C., and Manceau, A. (2019) Revealing the Chemical Form of
379 “Invisible” Gold in Natural Arsenian Pyrite and Arsenopyrite with High

380 Energy-Resolution X-ray Absorption Spectroscopy. ACS Earth and Space
381 Chemistry, 3, 1905–1914.
382 Ni, P., Pan, J.Y., Huang, B., Wang, G.G., Xiang, H.L., Yang, Y.L., Li, S.N., and Bao, T.
383 (2018) Geology, ore-forming fluid and genesis of the Qiucun gold deposit:
384 Implication for mineral exploration at Dehua prospecting region, SE China.
385 Journal of Geochemical Exploration, 195, 3–15.
386 Pačevski, A., Libowitzky, E., Zîvkovič, P., Dimitrijevič, R., and Cvetkovič, L. (2008)
387 Copper-bearing pyrite from the Coka Marin polymetallic deposit, Serbia: Mineral
388 inclusions or true solid-solution? Canadian Mineralogist, 46, 249–261.
389 Palenik, C.S., Utsunomiya, S., Reich, M., Kesler, S.E., Wang, L.M., and Ewing, R.C.
390 (2004) "Invisible" gold revealed: Direct imaging of gold nanoparticles in a
391 Carlin-type deposit. American Mineralogist, 89, 1359–1366.
392 Pring, A., Wade, B., McFadden, A., Lenehan, C.E., and Cook, N.J. (2020) Coupled
393 substitutions of minor and trace elements in co-existing sphalerite and wurtzite.
394 Minerals, 10, 147.
395 Reich, M., Kesler, S.E., Utsunomiya, S., Palenik, C.S., Chryssoulis, S.L., and Ewing,
396 R.C. (2005) Solubility of gold in arsenian pyrite. Geochimica et Cosmochimica
397 Acta, 69, 2781–2796.
398 Reich, M., Utsunomiya, S., Kesler, S.E., Wang, L.M., Ewing, R.C., and Becker, U.
399 (2006) Thermal behavior of metal nanoparticles in geologic materials. Geology,
400 34, 1033–1036.
401 Sharp, T.G., and Buseck, P.R. (1993) The distribution of Ag and Sb in galena:

Inclusions versus solid solution. American Mineralogist, 78, 85–95.

Shimazaki, H. (1980) Cooling history of orebody recorded in sphalerite: an example from the Tsumo skarn deposits, Japan. Journal of the Faculty of Science, University of Tokyo, Section II, 20, 61–76.

Slack, J.F., Neymark, L.A., Moscati, R.J., Lowers, H.A., Ransom, P.W., Hauser, R.L., and Adams, D.T. (2020) Origin of Tin Mineralization in the Sullivan Pb-Zn-Ag Deposit, British Columbia: Constraints from Textures, Geochemistry, and LA-ICP-MS U-Pb Geochronology of Cassiterite. Economic Geology, 115, 1699–1724.

Tagirov, B.R., Trigub, A.L., Kvashnina, K.O., Shiryaev, A.A., Chareev, D.A., Nickolsky, M.S., Abramova, V.D., and Kovalchuk, E. V. (2016) Covellite CuS as a matrix for “invisible” gold: X-ray spectroscopic study of the chemical state of Cu and Au in synthetic minerals. Geochimica et Cosmochimica Acta, 191, 58–69.

Wang, M.F., Zhang, X.B., Guo, X.N., Pi, D.H., and Yang, M.J. (2018) Silver-bearing minerals in the Xinhua hydrothermal vein-type Pb-Zn deposit, South China. Mineralogy and Petrology, 112, 85–103.

Williams-Jones, A.E., Bowell, R.J., and Migdisov, A.A. (2009) Gold in solution. Elements, 5, 281–287.

Wu, Z.W., Sun, X.M., Xu, H.F., Konishi, H., Wang, Y., Lu, Y., Cao, K.J., Wang, C., and Zhou, H.Y. (2018) Microstructural characterization and in-situ sulfur isotopic analysis of silver-bearing sphalerite from the Edmond hydrothermal field, Central Indian Ridge. Ore Geology Reviews, 92, 318–347.

Wu, Z.W., Sun, X.M., Xu, H.F., Konishi, H., Wang, Y., Wang, C., Dai, Y.Z., Deng, X.G., and Yu, M. (2016) Occurrences and distribution of "invisible" precious metals in sulfide deposits from the Edmond hydrothermal field, Central Indian Ridge. Ore Geology Reviews, 79, 105–132.

Xu, J., Cook, N.J., Ciobanu, C.L., Li, X.F., Kontonikas-Charos, A., Gilbert, S., and Lv, Y.H. (2021) Indium distribution in sphalerite from sulfide–oxide–silicate skarn assemblages: a case study of the Dulong Zn–Sn–In deposit, Southwest China. Mineralium Deposita, 56, 307–324.

Zhai, D.G., Liu, J.J., Cook, N.J., Wang, X.L., Yang, Y.Q., Zhang, A.L., and Jiao, Y.C. (2019) Mineralogical, textural, sulfur and lead isotope constraints on the origin of Ag-Pb-Zn mineralization at Bianjiadayuan, Inner Mongolia, NE China. Mineralium Deposita, 54, 47–66.

Zhang, H., Cai, Y.F., Gang, S., Brugger, J., Pring, A., Ni, P., Qian, G.J., Luo, Z.J., Zhang., Y., and Tan., W. (2022) Effects of arsenic on the distribution and mode of occurrence of gold during fluid–pyrite interaction: a case study of pyrite from the Qiucun gold deposit, China. American Mineralogist, 107, 914–929.

Zhang, Y., Cai, Y.F., Qu, Y., Wang, Q., Gu, L.X., and Li, G.J. (2020) Two-stage fluid pathways generated by volume expansion reactions: insights from the replacement of pyrite by chalcopyrite. Scientific reports, 2020, 10, 1–11.

Zhang, Y., Li, W.Q., Cai, Y.F., Qu, Y., Pan, Y.G., Zhang, W.L., and Zhao, K.D. (2021) Experimental investigation of the reactions between pyrite and aqueous Cu (I) chloride solution at 100–250°C. Geochimica et Cosmochimica Acta, 298, 1–20.

446 Zhao, J., Brugger, J., Grguric, B.A., Ngothai, Y., and Pring, A. (2017) Fluid-enhanced
447 coarsening of mineral microstructures in hydrothermally synthesized bornite–
448 digenite solid solution. ACS Earth and Space Chemistry, 1, 465–474.

449

450 **Figure Captions**

451 **Fig. 1.** (a) Photograph illustrating representative textures of a typical ore sample from
452 the Maluntou deposit. (b) TIMA image showing the mineral compositions within the
453 alteration zones. Abbreviations: Qtz = quartz, Sp = sphalerite, Ccp = chalcopyrite, Py
454 = pyrite, Gn = galena, Chl = chlorite, Fl = fluorite.

455 **Fig. 2.** Reflected light photomicrographs (a–b, e–g) and BSE images (c, d, h) of
456 Maluntou sulfides. (a) Image showing the intergrowths of galena and sphalerite.
457 Chalcopyrite occurs as blebs/lamellae in sphalerite (b, e–f) or fracture-fillings in
458 pyrite (g). Cu-Ag-(Au)-bearing nanoparticles are closely associated with chalcopyrite
459 inclusions (c–d) in sphalerite, and Ag-rich covellite with electrum (h) in pyrite, with
460 their EDS spectra shown in Fig. S2. Note that chalcopyrite inclusions are also
461 associated with pores in d. The regions of two TEM specimens (R1–R2) are
462 highlighted by white dashed boxes in b, and the boundaries between the
463 chalcopyrite-speckled- and the "barren" portions of sphalerite by yellow dashed lines
464 in e. Abbreviations are as per Fig. 1 with Elc = electrum and Cv = covellite.

465 **Fig. 3.** (a) Bright-field image showing the distortions within the chalcopyrite-rich
466 portions of sphalerite. HAADF-STEM images showing respectively associations of
467 chalcopyrite with native Cu (b), Cu-Ag-Au nanoalloy (c), and Cu-Ag-S nanoparticle

This is the peer-reviewed, final accepted version for American Mineralogist, published by the Mineralogical Society of America.
The published version is subject to change. Cite as Authors (Year) Title. American Mineralogist, in press.
DOI: https://doi.org/10.2138/am-2022-8636. http://www.minsocam.org/

(d), with the extension directions of chalcopyrite lamellae and distortions highlighted by white solid- and dashed arrows in c, respectively. (e) High-resolution STEM and fast Fourier transformation (FFT) images illustrating that the distortions in c follow sphalerite {111} planes. (f) Bragg-filtered image for e with some dislocations marked by white arrows. Abbreviations: DST = distortion, DSL = dislocation.

Fig. 4. STEM and EDS maps showing the distribution of Au-Ag-Cu nanoalloy. The Cu signal is partially from the TEM grid.

Figures

Figure 1

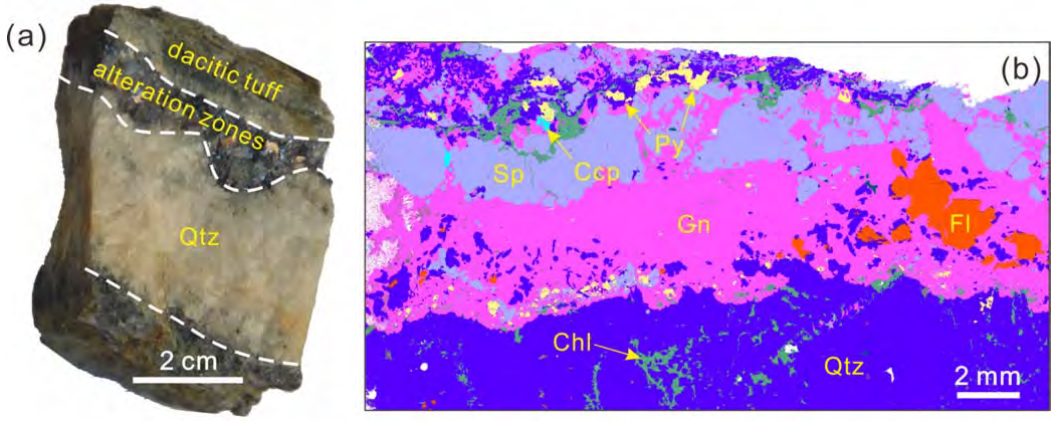

Figure 2

This is the peer-reviewed, final accepted version for American Mineralogist, published by the Mineralogical Society of America.
The published version is subject to change. Cite as Authors (Year) Title. American Mineralogist, in press.
DOI: https://doi.org/10.2138/am-2022-8636. http://www.minsocam.org/

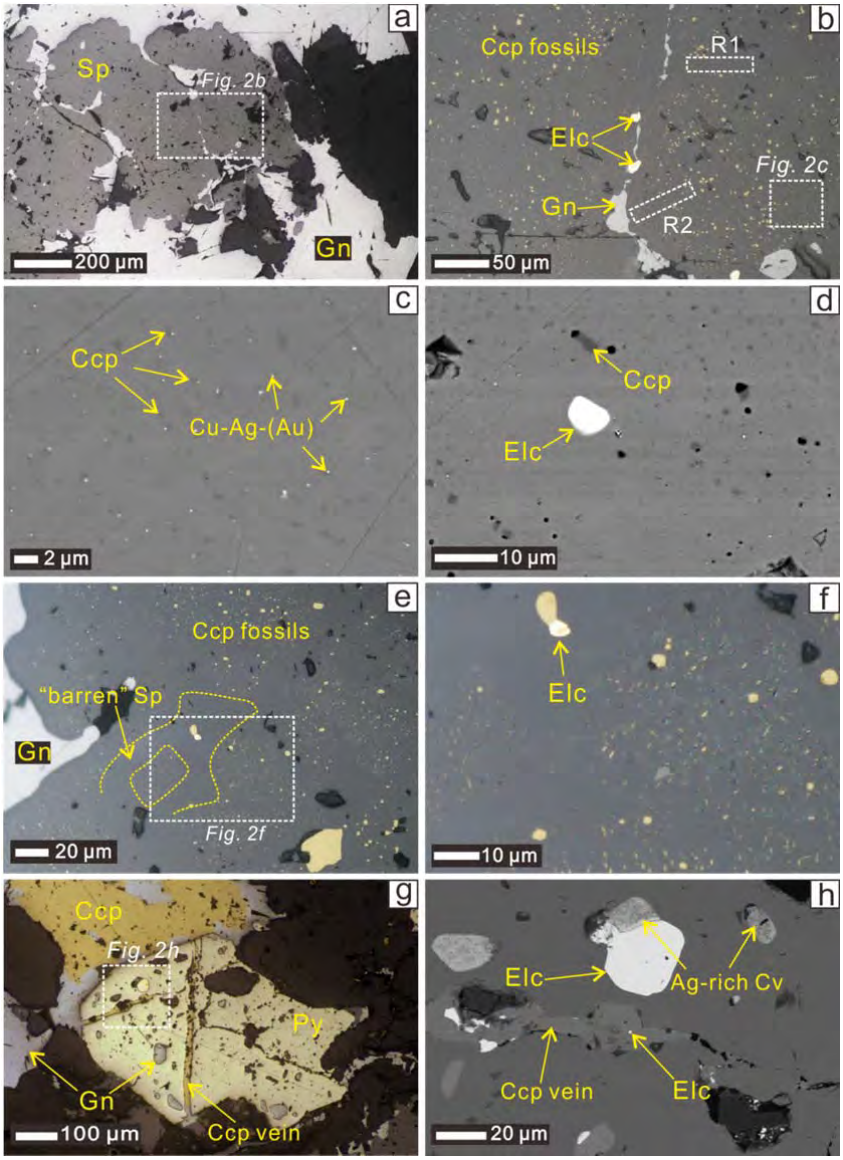

480

481 Figure 3

482

This is the peer-reviewed, final accepted version for American Mineralogist, published by the Mineralogical Society of America.
The published version is subject to change. Cite as Authors (Year) Title. American Mineralogist, in press.
DOI: https://doi.org/10.2138/am-2022-8636. http://www.minsocam.org/

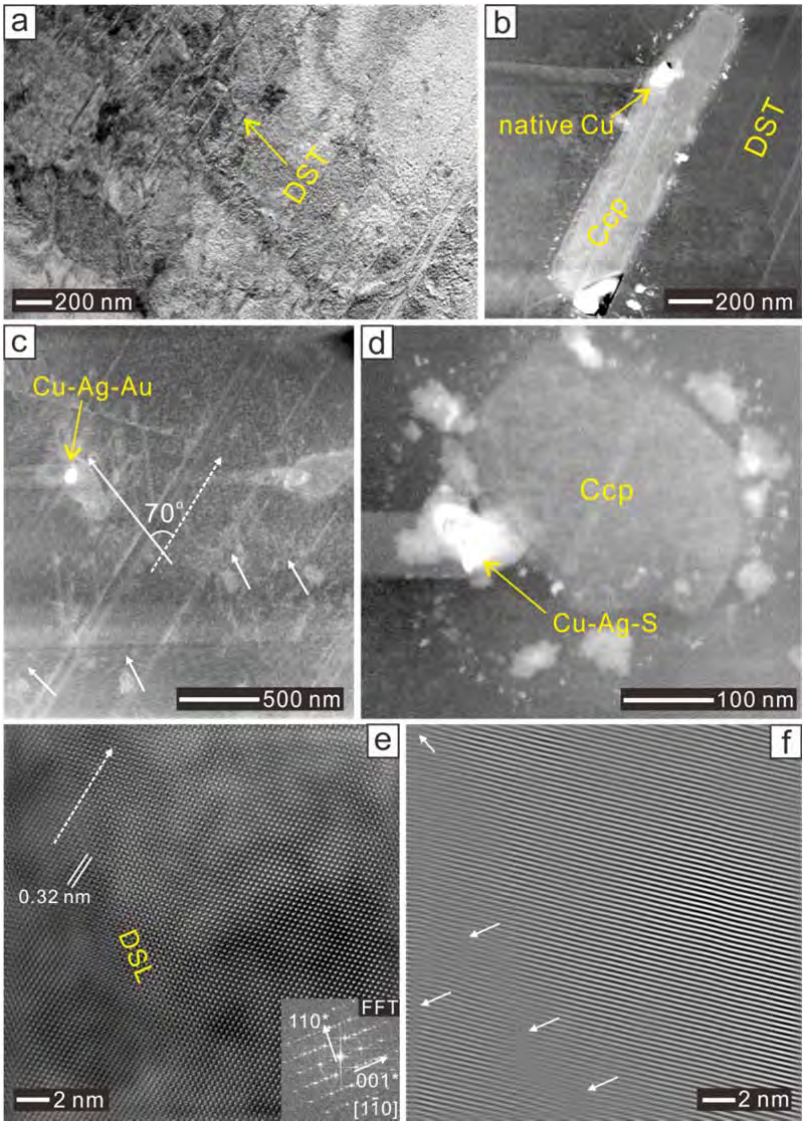

Figure 4

This is the peer-reviewed, final accepted version for American Mineralogist, published by the Mineralogical Society of America.
The published version is subject to change. Cite as Authors (Year) Title. American Mineralogist, in press.
DOI: https://doi.org/10.2138/am-2022-8636. http://www.minsocam.org/

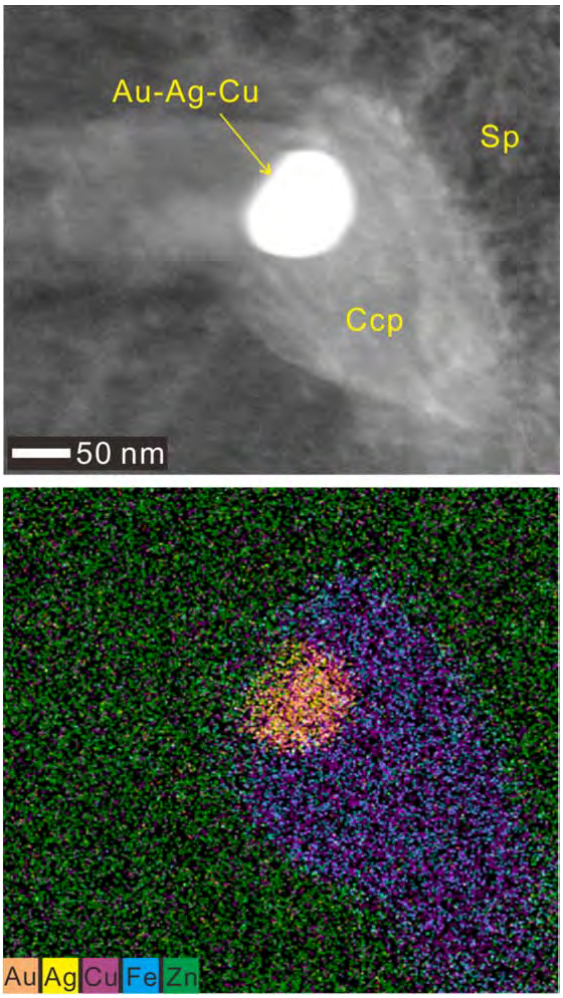

485

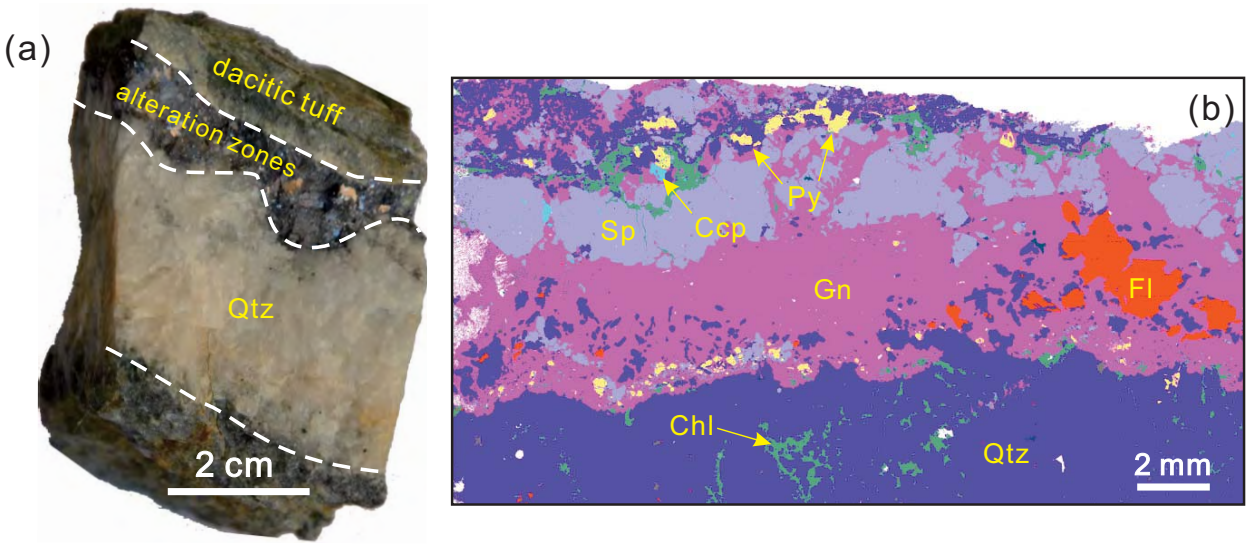

This is the peer-reviewed, final accepted version for American Mineralogist, published by the Mineralogical Society of America.
The published version is subject to change. Cite as Authors (Year) Title. American Mineralogist, in press.
DOI: https://doi.org/10.2138/am-2022-8636. http://www.minsocam.org/